ARTICLES SCIENCE CHINA Materials

mater.scichina.com link.springer.com

Published online 1 June 2017 | doi: 10.1007/s40843-017-9042-0
Sci China Mater 2017, 60(7): 646–653

Highly active CeO_2 hollow-shell spheres with Al doping

Zumin Wang[1†], Shuaiyu Jiang[1†], Yanhui Li[1], Pengfei Xu[1], Kun Zhao[1], Lingbo Zong[1], Hao Wang[2] and Ranbo Yu[1,2*]

ABSTRACT **Metal oxide hollow structures are of great interest in many current and emerging areas of technology. This paper presents a facile and controlled protocol for the synthesis of Al-doped CeO_2 hollow-shell spheres (CHS), where the dopant confers enhanced stability and activity to the material. These Al-doped CeO_2 hollow-shell spheres (ACHS) possess a controllable shell number of up to three, where the sizes of the exterior, middle, and interior spheres were about 250–100 nm,150–50 nm, and 40–10 nm, respectively, and the average shell thickness was ~15 nm. The thermal stability of the ACHS structure was enhanced by the homogeneous incorporation of Al atoms, and more active oxygen species were present compared with those in the non-doped congener. Au NPs supported on ACHS (Au/ACHS) showed superior catalytic performance for the reduction of *p*-nitrophenol. For the same Au NP content, the reaction rate constant (*k*) of the Au/ACHS was nearly twice that of the non-doped Au/CHS, indicating that Al doping is promising for improving the performance of inert or unstable oxides as catalyst supports.**

Keywords: CeO_2, hollow structure, doping, catalyst

INTRODUCTION

CeO_2 is recognized as an attractive candidate for advanced catalysis as well as an outstanding support material for noble metal nanoparticles (NPs), owing to its unique and remarkable physical/chemical properties, such as its numerous oxygen vacancy defects, high oxygen storage capacity, and facile interconversion between the trivalent and tetravalent oxidation states [1,2]. Furthermore, experimental and computational studies have proved that the surface defects of CeO_2 can strongly anchor and stabilize metal NPs or clusters through various strong interactions [3,4]. However, the non-stoichiometric defects in CeO_2 are not stable, even under very mild conditions. Thus, the concentration of the active oxygen species tends to decrease gradually, causing a sharp activity loss or even deactivation [5]. From a structural point of view, doping with low-valent cations (such as La^{3+} [6], Cu^{2+} [7], and Ni^{2+} [8]) may lead to the creation, ordering, and stabilization of oxygen vacancies [8], which has long been recognized as an important factor in determining the catalytic properties of materials [6,9,10]. Researchers have devoted tireless efforts to design effective strategies for manipulating the doping procedure, with the aim of optimizing the parameters for catalytic applications. The Al cation has proven to be a judicious choice based on its small ionic radius, which can enable the formation of more stable oxygen vacancies [11] and lead to higher surface areas [12]. Notably, among the many different dopants, Al is very effective for inhibiting sintering [13], which broadens the application scope of the materials at high temperature. Although several attempts have been made, finding a simple and controllable way to successfully dope Al into the CeO_2 lattice without the formation of mixed binary oxides [14] or unfavorable $CeAlO_3$ phases remains a formidable challenge [15].

Hollow structures constructed from tiny nanocrystals are of great scientific and practical value because they possess lower diffusion barrier limits and facilitate mass transport to and from the active sites [16,17], which is quite important for applications such as gas sensing [18], catalysis [19], energy storage [20,21], and drug delivery [22]. Among the various hollow structures, multi-shelled spheres are considered as one of the most promising and extraordinary candidates, especially for catalytic applications, due to their high-order, hollow, hierarchical structure, which may lead to functional materials with optimized properties [23]. These multi-shelled spheres possess a larger specific

[1] Department of Physical Chemistry, University of Science and Technology Beijing, Beijing 100083, China
[2] Centre for Future Materials, University of Southern Queensland, Queensland 4350, Australia
[†] These authors contributed equally to this work.
[*] Corresponding author (email: ranboyu@ustb.edu.cn)

surface area and pore volume, which provide an increased number of active sites and enhanced access for reactants to penetrate the structure [23]. Secondly, the multi-shelled hollow structure allows for more multiple reflections of the incident light, resulting in more efficient use of the light and enhanced catalytic activity in photoreactions [24]. Thirdly, the unique self-supported structure not only offers the advantages of the tiny NPs, but also provides the benefits of better buffering of volume changes and inner stress and strain to achieve excellent structural stability [25]. Last but not least, the unique hollow structure can efficiently trap noble metal NPs in the porous shells and the cavities, which allows better dispersion and facile immobilization, making this structure an ideal catalyst support [26,27]. Thus, the fabrication of various well-defined hollow spheres with multiple shells for catalysis is highly desirable.

Bearing all the above mentioned aspects in mind and motivated by the combined merits of morphology and function, we anticipated that better catalytic activity and stability of the Al-doped CeO_2 could be realized by generating a unique multi-shelled structure. Herein, a facile and reproducible synthetic strategy has been developed for the construction of multi-shelled hollow spheres of Al-doped CeO_2 (ACHS). Under the designed conditions, monodisperse and mesoporous doped CeO_2 multi-shelled spheres could be controllably obtained with large surface areas, well-defined morphologies, narrow size distributions, and good thermal stability. Remarkably, Al was successfully doped into CeO_2 to produce Al-doped CeO_2, rather than the two phase CeO_2-Al_2O_3 system, which created considerable surface defects such as Ce^{3+} and oxygen vacancies. As a consequence, very tiny gold (Au) NPs were evenly dispersed and anchored on these ACHS supports to generate the catalyst. The Au/ACHS catalysts show strikingly improved catalytic performance for the reduction of *p*-nitrophenol compared with their undoped counterparts.

EXPERIMENTAL SECTION

Chemicals, gases and materials

$Ce(NO_3)_3{\cdot}9H_2O$, $HAuCl_4{\cdot}4H_2O$, and *p*-nitrophenol were purchased from Sinopharm Chemical Reagent Co., Ltd. $Al(NO_3)_3{\cdot}6H_2O$, glucose, and $NaBH_4$ were purchased from Beijing Chemical Reagent Company. All the chemicals were analytically pure and were used without further purification.

Synthesis of carbonaceous spheres

The carbonaceous spheres were synthesized by a hydrothermal approach, as described in previous report [28]. Typically, 8 g of glucose was dissolved in 80 mL of deionized water, followed by hydrothermal reaction at 180°C for 24 h. The brown products were washed with deionized water and absolute alcohol alternately several times, then collected by centrifugation and dried at 80°C for 12 h.

Synthesis of ACHS

ACHS with different Ce:Al ratios were synthesized through a "hydrothermally enhanced adsorption and controlled calcination" method. The synthesis of Ce:Al = 10:1 ACHS is presented as an example. In this method, 50 mg of freshly prepared carbonaceous spheres was dispersed in 10 mL of deionized water under magnetic stirring. $Ce(NO_3)_3$ solution (0.5 mol L^{-1}, 10 mL) and $Al(NO_3)_3$ solution (0.5 mol L^{-1}, 1 mL) were added to the suspension. The mixture was adequately stirred for 45 min and then hydrothermally treated at 120°C for 6 h. Subsequently, the brown precursor was washed with deionized water and absolute alcohol several times, collected by centrifugation, and dried in air at 80°C. Finally, in order to obtain the ACHS, the precursor was calcined at 500°C for 1 h at a heating rate of 10°C min^{-1} under the air atmosphere of a tube furnace. The procedures used for preparation of the other ACHS samples were the same, except for the use of different amounts of metal salts as precursors. The obtained samples are referred to as CHS, and ACHS Ce:Al = 200:1, 50:1, 20:1, and 10:1, according to the initial feed ratio.

Synthesis of Au/ACHS hybrid nanostructure

The Au/ACHS hybrid nanostructure was fabricated *via* a method similar to that reported in our previous work [29]. In brief, 28 mg of the as-prepared ACHS was dispersed in 15 mL of deionized water under magnetic stirring. The freshly prepared $HAuCl_4$ (10 mmol L^{-1}, 500 μL) was added to the suspension and agitated for 18 h. The mixture was then collected by centrifugation, washed with deionized water, and redispersed in 30 mL of deionized water. Subsequently, freshly prepared $NaBH_4$ (30 mmol L^{-1}, 500 μL) was added to the mixture. The obtained purple powders were washed with deionized water until no chloride ions could be detected by the $AgNO_3$ test. Finally, the Au/ACHS hybrid nanostructures were dried under vacuum at 60°C.

Characterization

Powder X-ray diffraction (XRD) patterns were recorded on a PANalytical X' pert PRO instrument operated at 40 kV with Cu-Kα radiation (λ = 1.54184 Å). The scanning electron microscopy (SEM) images were acquired with

a field emission (FE)-SEM, ZEISS SUPRA^{TM55} instrument. The transmission electron microscopy (TEM) and high-resolution TEM (HRTEM) images were collected with a JEOL JEM-2100F instrument (accelerating voltage: 200 kV). The thermogravimetry-differential thermal analysis (TG-DTA) data were recorded using a Shimadzu TG/DTA6300 instrument at a linear heating rate of 10°C min^{-1} under air atmosphere. The X-ray photoelectron spectra (XPS) were recorded by an ESCALAB 250 Xi XPS system from Thermo Scientific with monochromatic Al-Kα radiation ($h\nu$ = 1486.6 eV). The binding energies for all spectra were calibrated with respect to the C 1s reference signal at 284.8 eV. Raman spectra were recorded using a JY HR800 laser Raman spectrometer with 532 nm excitation. Fourier-transform infrared (FTIR) spectra were obtained using a Fourier transform infrared spectrometer (Vector-22). The nitrogen adsorption-desorption isotherms were acquired at 77 K using a QuantachromeAutosorb-1 MP sorption analyzer. Samples were degassed under vacuum at 200°C overnight prior to analysis. Inductively coupled plasma-atomic emission spectrometry (ICP-AES) data were measured on an IRIS instrument (Intrepid IIXSP, Thermo Electron, USA) to determine the loading content of gold.

Catalytic evaluation test

The UV-vis spectra were acquired on a TU-1901UV-vis spectrophotometer from Beijing Purkinje General Instrument Co., Ltd. The catalytic activity was monitored directly by UV-vis spectrophotometry at room-temperature using a quartz cuvette. Freshly prepared *p*-nitrophenol (1 mmol L^{-1}, 150 μL) and $NaBH_4$ solution (100 mmol L^{-1}, 2 mL) were added, and then, an aqueous solution containing the Au/ACHS hybrid catalyst (1.4 mg mL^{-1}, 20 μL) was quickly injected into the cuvette to trigger the reaction. The intensity of the absorption peak of *p*-nitrophenol at 400 nm was monitored and recorded by UV-vis spectroscopy as a function of time.

RESULTS AND DISCUSSION

Based on the synthesis procedure and product analysis, a proposed mechanism for the formation of the triple-shelled hollow spheres is summarized and illustrated in Scheme 1. Firstly, under competitive adsorption, Ce and Al ions were captured by the surface functional groups and were trapped in the pores and channels of the porous carbonaceous spheres under hydrothermal treatment. Secondly, upon calcination, Ce and Al were redistributed in the carbonaceous spheres. As the temperature increased, the ions

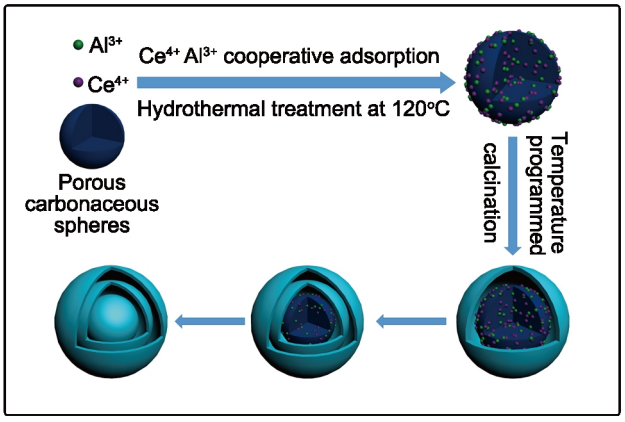

Scheme 1 Illustration of a possible mechanism for the formation of the Al-doped CeO_2 multi-shell hollow spheres.

penetrated deeper into the spheres before combustion of the organic species. Thirdly, with a further increase in the temperature, removal of the organic species and oxide crystallization occurred, which provided the driving force for separation of the shells. The precursors with different Ce and Al contents were obtained by competitive adsorption of the Ce and Al ions on the porous carbonaceous spheres under hydrothermal conditions at 120°C for 6 h. To obtain the final CHS and ACHS products, the precursors must be subjected to calcination. The calcination temperature was determined as 500°C from thermogravimetric (TG) analysis of the precursors (see the Supplementary information, Fig. S1). After calcination at 500°C for 1 h, the ACHS samples with different Ce:Al ratios were obtained.

The morphology and structure of the products were characterized by TEM. Fig. 1 (see Fig. S2 with larger magnification) shows that the as-synthesized CHS and ACHS products possess uniform spheres with three shells. The sizes of exterior, middle, and interior shells were about 250, 120, and 30 nm, respectively, whereas the average thickness of the shells was approximately 15 nm. Careful observation showed that all of the shells consist of very tiny nanocrystals. The XRD patterns of these CHS and ACHS (Fig. 2) species confirmed their phase purity, and all peaks matched well with those of pure cubic fluorite ceria (PDF card 34-394). Moreover, as the starting Ce:Al ratio decreased, the crystallinity of the products decreased, which may indicate that the presence of Al can prevent aggregation and growth of the primary particles of the CeO_2 crystals that comprise the multi-shelled structure during calcination. In order to establish the relationship between Al doping and variation of the cell parameters, XRD data were acquired, as summarized in Table S1. The

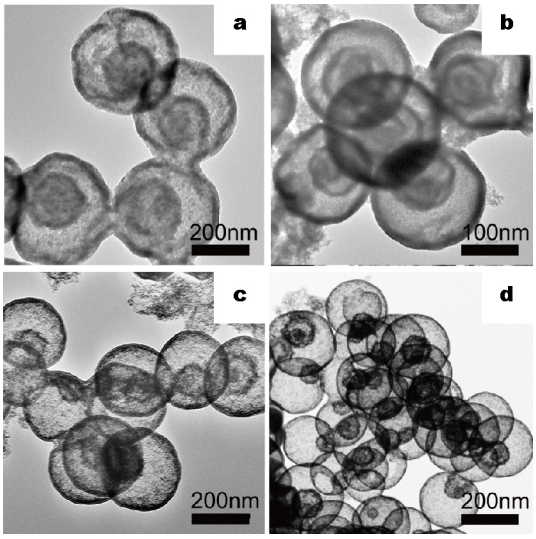

Figure 1 TEM images of the hollow spheres: (a) CeO_2 triple shell spheres; (b) Ce:Al = 200:1, (c) Ce:Al = 50:1, (d) Ce:Al = 10:1.

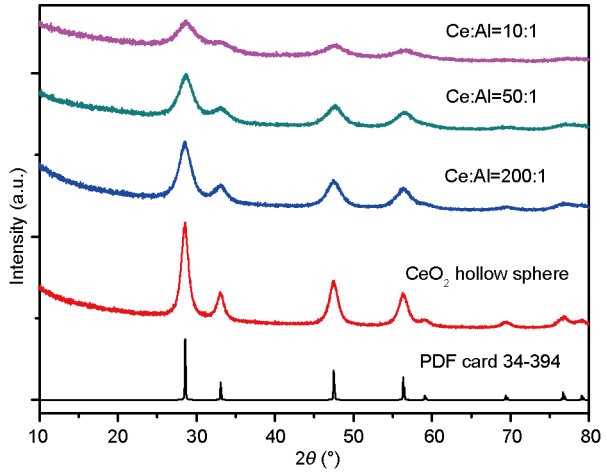

Figure 2 XRD patterns of the hollow spheres with different Ce:Al ratios.

results show that with an increase in the concentration of the Al dopant, the peaks tended to move toward higher angle, indicating a slight increase in the lattice parameter, which provides evidence in support of the successful Al doping into the lattice.

To further identify the presence of Al, XRD patterns of the sample with an initial Ce:Al ratio of 10:1 calcined at 1000°C for 1 h was collected (Fig. S3). The data suggest that the cubic fluorite structure was conserved with no additional peaks, which indicates that the Al dopant is not in the form of Al_2O_3 or $CeAlO_3$.

The final molar ratio of Ce and Al in each sample was determined through energy-dispersive X-ray spectroscopic (EDS) analysis and confirmed by ICP-MS. The results (see Fig. S4 and Table S2) show that the final Ce:Al ratio ranged from 2.70 to 0.66, which is much less than the starting ratio, whereas the same trend is maintained. This may be mainly because the radius of the Al ion (0.0535 nm) is much smaller than that of the Ce ion (0.1034 nm); thus, Al^{3+} is much more easily adsorbed into the carbonaceous spheres.

In order to further study the states of Ce and Al in the sample, XPS analysis of the CHS and ACHS samples was conducted (Figs S5 and S6). Fig. S5a shows the Ce 3d peaks of the three different samples; there is a slight change for the sample with the starting Ce:Al ratio of 50:1. To further understand the change, the fitting results are shown in Fig. S6. All samples gave rise to ten peaks, but it is noteworthy that the concentration of Ce^{3+} increased with the doping of Al [30]. When the starting Ce:Al ratio reached 50:1, the Ce^{3+} concentration increased significantly, moving from 17.1% to 31.2% (Table 1). Fig. S5b–e show the fitting results for the O 1s spectra. The O 1s spectra were deconvoluted into two peak contributions, referred to as the O_I and O_{II} components. The major peak of component O_I with a binding energy (BE) of 529.3–529.6 eV is characteristic of lattice oxygen. Component O_{II} with BE≈531.4–531.7 eV is attributed to active oxygen species [21] (most likely oxygen vacancies [30,31] and adsorbed oxygen molecules [32,33]). Obviously, with a decrease in the Ce:Al ratio, the relative intensity of the O_{II} to O_I peaks became stronger, which means the active species increased from 26.78% to 70.22%. This result matches with the trend in the increase of Ce^{3+}, because the formation of oxygen-vacancies is considered as an elementary step in the reduction of Ce^{4+}. This agrees with the well-known property of CeO_2 when doped with aliovalent cations, such as La^{3+} [18]. The Al 2p spectra for the Ce:Al = 200:1 and Ce:Al = 50:1 (Fig. S7) samples show one peak, respectively, at around 73.7 eV, which can be attributed to Al^{3+} [24]. This exciting result demonstrates that by proper Al(III) doping into CeO_2, a dramatic enhancement of the surface active species can be achieved.

It was found that when the as-prepared CeO_2 multi-shell spheres were doped with Al, the thermal stability was im-

Table 1 Comparison of the XPS fitting data for $Ce^{3+}/(Ce^{4+}+Ce^{3+})$ and $O_{II}/(O_I+O_{II})$ for different samples

Sample	Ce:Al	$Ce^{3+}/(Ce^{3+}+Ce^{4+})$ (%)	$O_{II}/(O_I+O_{II})$ (%)
1	CeO_2	17.1	26.78
2	200:1	17.4	40.15
3	50:1	31.2	60.55
4	20:1	32.6	64.82
5	10:1	35.7	70.22

proved considerably. Fig. S10a, c, e shows the *in situ* high-temperature XRD patterns of the CeO_2 hollow spheres, Ce:Al = 200:1 hollow spheres, and Ce:Al = 10:1 hollow spheres, respectively. Fig. S10b, d, f show the corresponding magnified profile of the peak at about 28.5° for the respective samples. The comparative experiments were performed under the same conditions (as shown in the Supplementary information). In the case of CHS (Fig. S10a, b), the peak began to become sharper at 500°C, and when the temperature reached 800°C, the pattern showed a very obvious change. For the samples with Ce:Al ratios of 200:1 and 10:1 (Fig. S10c–f), the patterns remained unchanged up to 650°C, which is much higher than the corresponding temperature for CHS; at 800°C, the change was moderate. The full widths at half maximum (FWHMs) of all patterns are summarized in Table S3. With an increase in the Al loading, the thermal resistance became even more pronounced. The combination of the activity and stability of this material may greatly broaden its application scope, especially for use at high-temperature.

For the catalytic reaction, the porous feature and specific area are of vital importance. The N_2 adsorption-desorption isotherms of the hollow spherical samples with starting Ce:Al ratios of 200:1, 50:1, and 10:1 are given in the Supplementary information (Fig. S11). The Brunauer-Emmett-Teller (BET) specific areas of these ACHS were 88.7, 96.4 and 104.6 $m^2 g^{-1}$, respectively. The Barrett-Joyner-Halenda (BJH) pore size distribution curves in the inset demonstrate the presence of mesoporous structures.

The large specific surface area, sufficient active sites, and high thermal stability of these ACHS samples make them promising supports for loading noble metals to construct high-performance catalysts. Herein, an impregnation-reduction method was used to construct the Au/ACHS hybrid nanostructured catalyst. Fig. S12a shows that the Au NPs were well-dispersed around the shell of the ACHS support. Fig. S12b shows that the Au NPs were strongly attached to the ACHS support with a diameter of about 5 nm. The loading content of gold for all three different samples was about 3 wt.%, as determined by ICP analysis.

The reduction of *p*-nitrophenol by sodium borohydride is widely used as a model reaction to evaluate the catalytic ability of noble metal (Au, Pt, and Pd)-supported catalysts, since this reaction does not progress at room temperature without a catalyst [34,35]. As the reaction took place, the characteristic absorption peak of *p*-nitrophenol at 400 nm gradually disappeared, whereas the characteristic absorption peak of *p*-aminophenol became stronger (Fig. 3a and Fig. S13a, b). The C_t to C_0 parameters describe the *p*-nitrophenol concentration at time *t* and at 0 min, respectively. The reaction rate constant *k* was determined from the slope of the plots of $\ln(C_t/C_0)$ *vs.* time. The reaction rates of CHS and ACHS with starting Ce:Al ratios of 200:1, 50:1, and 10:1 and the CeO_2 powder without the hollow structure are shown in Fig. 3b. The results followed the order: 50:1ACHS > 10:1ACHS> 200:1ACHS > CHS >> CeO_2 powder, which revealed that Al doping led to a significant enhancement of the catalytic properties, where the optimal composition was Ce:Al = 50:1. This may result from the stronger Au/support interaction. As discussed earlier in relation to the XPS fitting results, with an increase in the Al doping, the surface defects (such as oxygen vacancies, Ce^{3+}) increased distinctly. With an increase in the amount of surface defects, CeO_2 can strongly bind metal NPs or nanoclusters (NCs) [4] by enhanced electronic interaction between CeO_2 and the supported metal NPs [36,37]. Moreover, a synergetic effect may be derived from modification of the *d*-band center [38], resulting in formation of smaller Au NPs that are not only highly active but also distinctively stable under realistic reaction conditions [39]. This in turn may have significant catalytic consequences in terms of the number and type of active sites exposed. However, when the doping ratio was further increased to 10:1, the excessive Al doping may have weakened the synergistic effect between the Au NPs and CeO_2, thus compromising the activity. The obtained catalysts were also adequately stable and their activities and morphologies were preserved after ten successive cycles (Fig. S14). All of these features, along with our preliminary promising results, indicate the significant potential for the controllable synthesis of doped oxides with multi-shells. Further investigations of the applications of this catalyst system in heterogeneous catalysis are thus warranted. Future work will involve application of these catalysts to reactions such as CO oxidation and oxygen storage-release to achieve high reactivity and sintering resistance, especially at high temperature.

CONCLUSIONS

In summary, well-dispersed Al-doped CeO_2 multi-shell hollow spheres with a large specific surface area, sufficient active sites, and high thermal stability were successfully fabricated using porous carbonaceous spheres as hard templates. Through a facile "hydrothermally-enhanced competitive adsorption and controlled calcination" method [40], Al was homogeneously introduced into the CeO_2 lattice to create numerous active oxygen species.

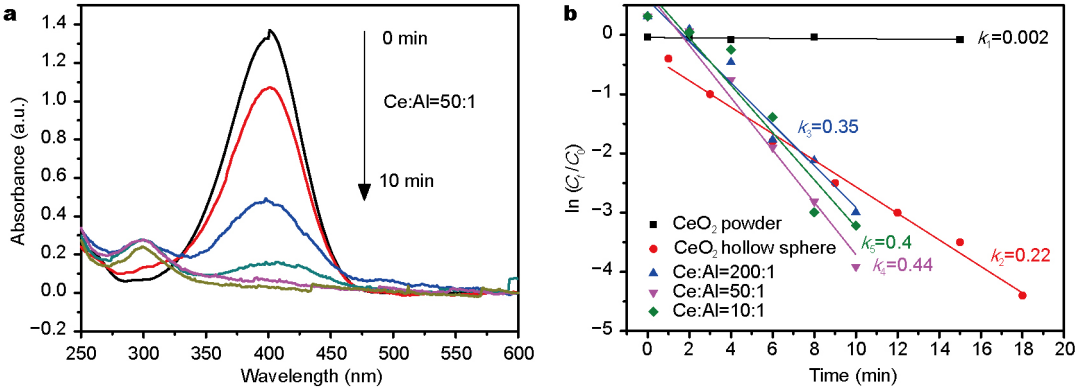

Figure 3 UV-vis spectra for the catalytic reduction of *p*-nitrophenol to *p*-aminophenol on Au/ACHS with different Al contents. (a) Absorption of *p*-nitrophenol and *p*-aminophenol for the hollow spherical sample with Ce:Al ratio of 200:1; (b) the reaction rates of CHS and ACHS with Ce:Al ratios of 200:1, 50:1, and 10:1 and the CeO_2 powder without the hollow structure.

Upon supporting Au NPs, the Au/ACHS catalysts showed much higher activity than the non-doped Au/CHS catalyst. This present work contributes not only to the methodology or synthesis of complex hollow structures, but also the development of a powerful approach for improving the performance of inert or unstable oxides as catalyst supports.

Received 13 March 2017; accepted 2 May 2017; published online 1 June 2017

1 Sun C, Li H, Chen L. Nanostructured ceria-based materials: synthesis, properties, and applications. Energ Environ Sci, 2012, 5: 8475–8505
2 Lawrence NJ, Brewer JR, Wang L, *et al.* Defect engineering in cubic cerium oxide nanostructures for catalytic oxidation. Nano Lett, 2011, 11: 2666–2671
3 Branda MM, Loschen C, Neyman KM, *et al.* Atomic and electronic structure of cerium oxide stepped model surfaces. J Phys Chem C, 2008, 112: 17643–17651
4 Zhang C, Michaelides A, Jenkins SJ. Theory of gold on ceria. Phys Chem Chem Phys, 2011, 13: 22–33
5 Zhao K, Qi J, Yin H, *et al.* Efficient water oxidation under visible light by tuning surface defects on ceria nanorods. J Mater Chem A, 2015, 3: 20465–20470
6 Skorodumova NV, Simak SI, Lundqvist BI, *et al.* Quantum origin of the oxygen storage capability of ceria. Phys Rev Lett, 2002, 89: 166601
7 Pu ZY, Liu XS, Jia AP, *et al.* Enhanced activity for CO oxidation over Pr- and Cu-doped CeO_2 catalysts: effect of oxygen vacancies. J Phys Chem C, 2008, 112: 15045–15051
8 Kehoe AB, Scanlon DO, Watson GW. Role of lattice distortions in the oxygen storage capacity of divalently doped CeO $_2$. Chem Mater, 2011, 23: 4464–4468
9 Li C, Xin Q, Guo X. Surface oxygen species and their reactivities in the mild oxidation of ethylene on cerium oxide studied by FT-IR spectroscopy. Catal Lett, 1992, 12: 297–305
10 Trovarelli A. Catalytic properties of ceria and CeO_2-containing materials. Catal Rev, 1996, 38: 439–520
11 Nolan M. Charge compensation and Ce^{3+} formation in trivalent doping of the CeO_2 (110) surface: the key role of dopant ionic radius. J Phys Chem C, 2011, 115: 6671–6681
12 Yuzhakova T, Rakić V, Guimon C, *et al.* Preparation and characterization of Me_2O_3–CeO_2 (Me=B, Al, Ga, In) mixed-oxide catalysts. Chem Mater, 2007, 19: 2970–2981
13 Pijolat M, Prin M, Soustelle M, *et al.* Thermal stability of doped ceria: experiment and modelling. Faraday Trans, 1995, 91: 3941–3948
14 Ilieva-Gencheva L, Pantaleo G, Mintcheva N, *et al.* Nano-structured gold catalysts supported on CeO_2 and CeO_2-Al_2O_3 for NO_x reduction by CO: effect of catalyst pretreatment and feed composition. J Nanosci Nanotech, 2008, 8: 867–873
15 Yao H. Ceria in automotive exhaust catalysts I. Oxygen storage. J Catal, 1984, 86: 254–265
16 Lou XWD, Archer LA, Yang Z. Hollow micro-/nanostructures: synthesis and applications. Adv Mater, 2008, 20: 3987–4019
17 Zhang H, Zhu Q, Zhang Y, *et al.* One-pot synthesis and hierarchical assembly of hollow Cu_2O microspheres with nanocrystals-composed porous multishell and their gas-sensing properties. Adv Funct Mater, 2007, 17: 2766–2771
18 Lee JH. Gas sensors using hierarchical and hollow oxide nanostructures: overview. Sensors Actuators B-Chem, 2009, 140: 319–336
19 Cui P, Wang J, Wang Z, *et al.* Bismuth oxychloride hollow microspheres with high visible light photocatalytic activity. Nano Res, 2016, 9: 593–601
20 Wang Z, Zhou L, David Lou XW. Metal oxide hollow nanostructures for lithium-ion batteries. Adv Mater, 2012, 24: 1903–1911
21 Li S, Li A, Zhang R, *et al.* Hierarchical porous metal ferrite ball-in-ball hollow spheres: general synthesis, formation mechanism, and high performance as anode materials for Li-ion batteries. Nano Res, 2014, 7: 1116–1127
22 An K, Hyeon T. Synthesis and biomedical applications of hollow nanostructures. Nano Today, 2009, 4: 359–373
23 Qi J, Lai X, Wang J, *et al.* Multi-shelled hollow micro-/nanostructures. Chem Soc Rev, 2015, 44: 6749–6773
24 Liu H, Ma H, Joo J, *et al.* Contribution of multiple reflections to light utilization efficiency of submicron hollow TiO_2 photocatalyst. Sci China Mater, 2016, 59: 1017–1026
25 Wang J, Tang H, Zhang L, *et al.* Multi-shelled metal oxides prepared via an anion-adsorption mechanism for lithium-ion batteries. Nat Energ, 2016, 1: 16050
26 Zhao K, Qi J, Zhao S, *et al.* Multiple Au cores in CeO_2 hollow spheres for the superior catalytic reduction of *p*-nitrophenol. Chin J Catal, 2015, 36: 261–267
27 Keilitz J, Schwarze M, Nowag S, *et al.* Homogeneous stabilization of

Pt nanoparticles in dendritic core-multishell architectures: application in catalytic hydrogenation reactions and recycling. ChemCatChem, 2010, 2: 863–870
28 Sun X, Li Y. Colloidal carbon spheres and their core/shell structures with noble-metal nanoparticles. Angew Chem Int Ed, 2004, 43: 597–601
29 Xu P, Yu R, Ren H, *et al.* Hierarchical nanoscale multi-shell Au/CeO_2 hollow spheres. Chem Sci, 2014, 5: 4221–4226
30 Wang Y, Wang F, Chen Y, *et al.* Enhanced photocatalytic performance of ordered mesoporous Fe-doped CeO_2 catalysts for the reduction of CO_2 with H_2O under simulated solar irradiation. Appl Catal B-Environ, 2014, 147: 602–609
31 Larachi F, Pierre J, Adnot A, *et al.* Ce 3d XPS study of composite $Ce_xMn_{1-x}O_{2-y}$ wet oxidation catalysts. Appl Surface Sci, 2002, 195: 236–250
32 Huang X, Beck MJ. Size-dependent appearance of intrinsic O_x^q "activated oxygen" molecules on ceria nanoparticles. Chem Mater, 2015, 27: 5840–5844
33 Dos Santos ML, Lima RC, Riccardi CS, *et al.* Preparation and characterization of ceria nanospheres by microwave-hydrothermal method. Mater Lett, 2008, 62: 4509–4511
34 Huang X, Guo C, Zuo J, *et al.* An assembly route to inorganic catalytic nanoreactors containing sub-10-nm gold nanoparticles with anti-aggregation properties. Small, 2009, 5: 361–365
35 Panigrahi S, Basu S, Praharaj S, *et al.* Synthesis and size-selective catalysis by supported gold nanoparticles: study on heterogeneous and homogeneous catalytic process. J Phys Chem C, 2007, 111: 4596–4605
36 Zhang C, Michaelides A, King DA, *et al.* Structure of gold atoms on stoichiometric and defective ceria surfaces. J Chem Phys, 2008, 129: 194708–194708
37 Zhang C, Michaelides A, King DA, *et al.* Anchoring sites for initial au nucleation on CeO_2 {111}: O vacancy *versus* Ce vacancy. J Phys Chem C, 2009, 113: 6411–6417
38 Zhang J, Chen G, Guay D, *et al.* Highly active PtAu alloy nanoparticle catalysts for the reduction of 4-nitrophenol. Nanoscale, 2014, 6: 2125–2130
39 Ta N, Liu JJ, Chenna S, *et al.* Stabilized gold nanoparticles on ceria nanorods by strong interfacial anchoring. J Am Chem Soc, 2012, 134: 20585–20588
40 Sun Z, Liao T, Kou L. Strategies for designing metal oxide nanostructures. Sci China Mater, 2017, 60: 1–24

Acknowledgments This work was financially supported by the National Natural Science Foundation of China (51472025 and 21671016) and Beijing Nova Programme Interdisciplinary Cooperation Project.

Author contributions Wang Z designed and engineered the samples; Jiang S and Li Y performed the experiments; Wang Z wrote the paper with support from Jiang S. All authors contributed to the general discussion.

Conflict of interest The authors declare that they have no conflict of interest.

Supplementary information Supporting data are available in the online version of the paper.

Zumin Wang received his BE degree from the School of Metallurgical and Ecological Engineering, the University of Science and Technology, Beijing (USTB) in 2012. He is currently studying for his PhD degree under the supervision of Prof. Ranbo Yu from the Laboratory of Physical Chemistry of Materials Preparation at the Department of Physical Chemistry, USTB. His current research interests are focused on the design and synthesis of micro-/nanostructured functional inorganic nanomaterials for catalysis.

Shuaiyu Jiang received his BE degree from the University of Science and Technology Liaoning (2013) and MSc from the USTB (2016). He is currently a PhD candidate at the Griffith University. His current research interest is focused on the synthesis of micro-/nanostructured photocatalyst.

Ranbo Yu received her BSc and MSc degrees at Jilin University (1994 and 1997) and PhD at Yamanashi University (2002). As a postdoctoral researcher she worked in Kyoto University (JSPS fellow) and the University of Houston in 2002 and 2003. She currently holds a professor position at the Department of Physical Chemistry, USTB. Her research interests focus on the development of micro-/nanostructured functional inorganic materials and their applications in catalysis.

铝掺杂氧化铈多壳层空心球的可控合成及其催化应用

王祖民[1†], 姜帅宇[1†], 李彦辉[1], 徐鹏飞[1], 赵昆[1], 宗玲博[1], 王浩[2], 于然波[1,2*]

摘要 本文利用多孔碳球为模板, 通过竞争吸附控制煅烧法制备了铝掺杂的氧化铈多壳层空心球材料. 通过XRD、SEM、TEM对所得材料的结构、表面形貌以及热稳定性能进行了表征, 结果表明该方法制备的不同掺杂比例的多壳层空心球均一分散, 铝原子被均匀地分布到氧化铈的晶格中, 使其热稳定性得到提高. XPS结果表明铝的掺杂大大提高了材料中三价铈和表面氧空位的比例, 所以当其被作为催化剂载体时, 负载的金纳米粒子更加分散且与载体结合作用更强. 将该催化剂应用于硝基苯酚加氢反应, 其催化活性比未掺杂铝的样品提高了一倍. 本文研究结果表明铝掺杂可以有效提高氧化铈催化剂的稳定性和活性; 竞争吸附控制煅烧法是制备空心掺杂材料的一种简单实用的方法.